

ARTICLE OPEN



Combined large-scale tropical and subtropical forcing on the severe 2019–2022 drought in South America

J. L. Geirinhas¹✉, A. C. Russo¹, R. Libonati^{1,2}, D. G. Miralles¹, A. M. Ramos⁴, L. Gimeno¹, R. M. Trigo^{1,2}

Changes in the frequency and magnitude of dry spells have been recorded over the past few decades due to an intensification of the global water cycle. A long-term soil drying trend resulting from a joint contribution of natural decadal variability in precipitation levels and increasing temperatures, predisposed central-east South America (CESA) to experience during 2019–2022 a period of outstanding soil desiccation. Flash droughts led to large areas ($\sim 100,000 \text{ km}^2$) in CESA covered by record-breaking soil dryness. April 2020 witnessed the most severe conditions, when over 30% of the region experienced negative soil moisture anomalies larger than two standard deviations. Internal variability, particularly El Niño–Southern Oscillation, explained the dynamical forcing of this extreme drought. Large precipitation deficits and enhanced evaporation in CESA resulted from a coupled tropical and subtropical forcing associated to pronounced changes in the normal Walker and Hadley Cells' circulation and to the establishment of a Rossby wave extending from west south Pacific towards South America. These findings highlight the intricate interplay between different mechanisms in the occurrence of climate extremes, stressing the need for an adequate representation of the dynamical processes associated with daily-to-multiyear timescales in climate models.

npj Climate and Atmospheric Science (2023)6:185; <https://doi.org/10.1038/s41612-023-00510-3>

INTRODUCTION

Climate change is expected to cause, through both thermodynamic and dynamical mechanisms, a strengthening of the global water cycle and thus profound changes in the frequency and magnitude of dry and wet spells^{1–3}. This poses great pressure on global freshwater availability^{4,5}, food security⁶ and sustainability of natural ecosystems⁷. Higher levels of lower-tropospheric water vapor promoted by increasing temperatures, are linked to changes in the balance between evaporation and precipitation (E-P) that ultimately determines soil moisture, groundwater recharge and total water available for runoff^{8–10}. Long-term drying trends can influence the atmospheric water budget, particularly over drylands, by limiting evaporation and reducing moisture recycling for precipitation^{10–13}. On the other hand, reduced soil moisture conditions may also enhance, through convective instability, the atmospheric moisture convergence contributing to a higher frequency of extreme precipitation episodes from convective storms^{10,14–16}. In parallel, under a large atmospheric evaporative demand, a strong soil moisture imbalance may also play a major role in the surface energy partitioning by constraining surface latent heat fluxes, leading to an above-normal accumulation of sensible heat in the atmosphere and to the escalation of temperatures^{17–19}. Thus, the interplay between soil moisture, atmospheric water budget and temperature is part of a large and complex framework of feedbacks that are modulated by climate change (i.e., increasing temperatures, changes in vegetation and in atmospheric dynamics), and that may also affect the climate trends themselves^{10,14,20}.

So far, relatively little attention has been given to the simultaneous assessment of temperature, precipitation and soil moisture trends over South America (SA)²¹. According to the last report from the Intergovernmental Panel on Climate Change

(IPCC)²², most of the continent has warmed up at a rate between 0.1 °C and 0.4 °C per decade during the 1981–2020 period, with tropical SA experiencing the largest warming trends. Previous studies have also pointed to a significant increase in the frequency of warm extremes during the 1961–2018 period^{23,24}. Regarding precipitation, the conclusions are less spatially coherent and the projections for SA indicate a dipole pattern of drier conditions centered in the Amazon, while wetter conditions prevail in central-eastern parts of the continent, i.e., over La Plata Basin^{25,26}. The evaporation from the Amazon and La Plata basins (Fig. 1a), the two largest watersheds of SA, is crucial for the regional hydroclimate and for precipitation through local moisture recycling and moisture transport between both^{27–29}. Other external moisture sources are also important for the atmospheric water budget over these two watersheds, such as the large quantities of water vapor transported from the Atlantic into the Amazon Basin by the trade winds^{27,28}. All these hydrological processes are modulated by a complex interplay between large-scale oceanic-atmospheric modes of variability such as the El Niño–Southern Oscillation (ENSO)^{30,31}, the Madden–Julian Oscillation (MJO)^{32,33} and the Atlantic Meridional and Zonal Modes (AMM and AZM, respectively)²⁹. These climate variability modes influence semi-permanent and transient systems that play a key role for precipitation and evaporation in SA, namely the Inter-Tropical Convergence Zone, the South Atlantic Convergence Zone, the South America Low Level Jet (SALLJ), mid-latitude cold fronts, cyclones and quasi-stationary anticyclonic systems^{30,34}.

More recently, La Plata basin and Pantanal in central-east South America (CESA), have been affected by a severe drought whose first signs were noticed during mid-2018 in Southeast Brazil³⁵. However, soil dryness rapidly extended to adjacent areas in Paraguay, Bolivia, and later over northern Argentina, where

¹Universidade de Lisboa, Faculdade de Ciências, Instituto Dom Luiz, 1749-016 Lisboa, Portugal. ²Departamento de Meteorologia, Universidade Federal do Rio de Janeiro, Rio de Janeiro 21941-919, Brazil. ³Hydro-Climate Extremes Lab (H-CEL), Ghent University, Sint-Pietersnieuwstraat, Belgium. ⁴Institute for Meteorology and Climate Research (IMK-TRO), Karlsruhe Institute of Technology (KIT), Karlsruhe, Germany. ⁵Centro de Investigación Mariña, Universidad de Vigo, Environmental Physics Laboratory (EPhysLab), Ourense, Spain.
✉ email: jlgeirinhas@fc.ul.pt

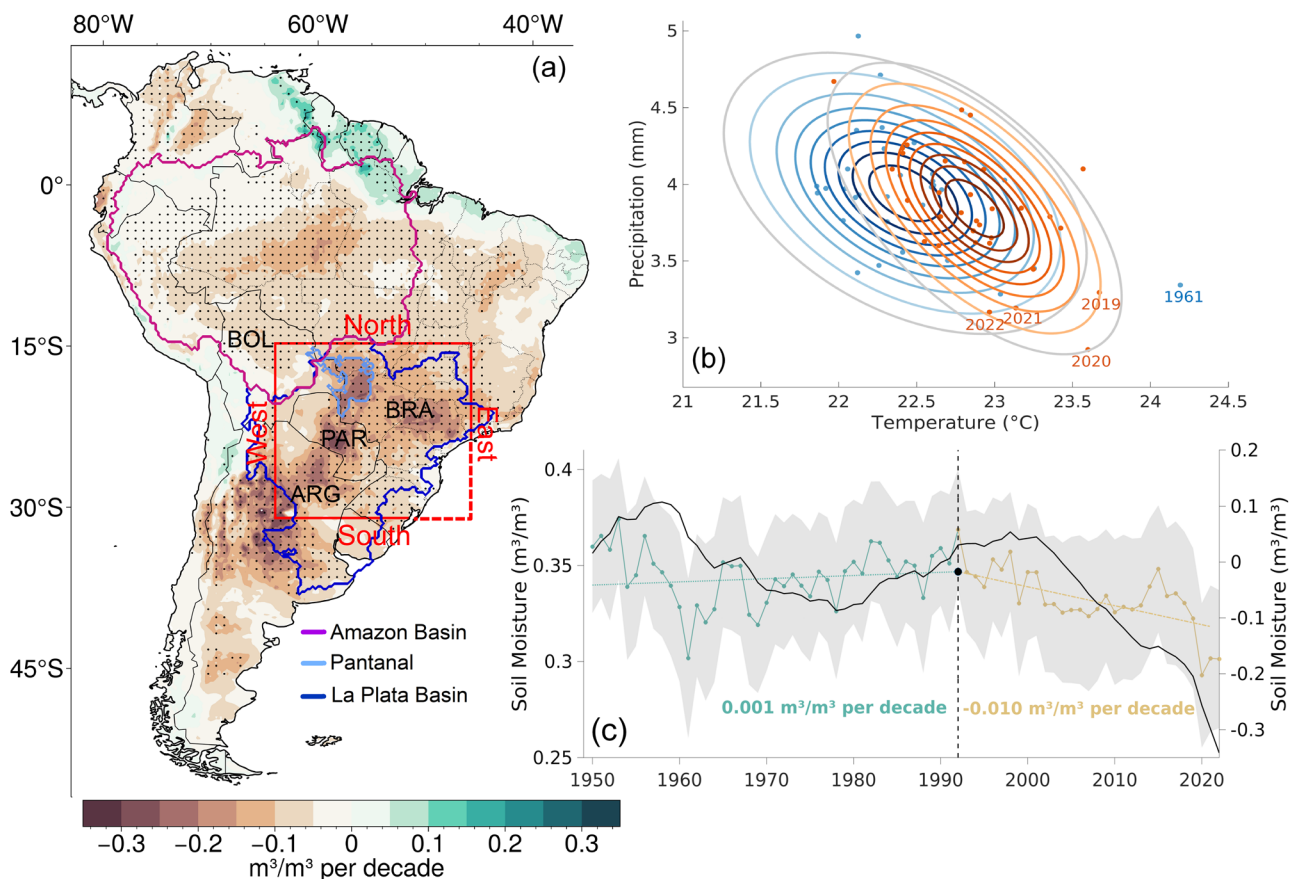


Fig. 1 Long-term drying trends over SA. a Spatial distribution over SA of soil moisture trends (m^3/m^3 per decade) over the 1990–2022 period. The black dots depict regions with statistically significant trends at a 5% level, according to the non-parametric Mann-Kendall two-tailed test. The limits of the Amazon basin, La Plata Basin and the Pantanal biome are marked by the purple, blue and turquoise lines, respectively. The red box delimits the region of interest covering CESA. **b** Bivariate Gaussian probability distribution functions of mean annual surface temperatures ($^{\circ}\text{C}$) and daily accumulated precipitation levels (mm) averaged over CESA, for the 1959–1989 (blue ellipses) and the 1990–2022 periods (orange ellipses). The gray ellipses show the 95% level of the probability distribution. **c** Time series (1951–2022) of mean annual soil moisture levels, spatially averaged over CESA (green and yellow lines, left y-axis), and of the time accumulated soil moisture anomalies regarding the climatological period of 1981–2010 (black line, right y-axis). The dash green and yellow lines result from a regression model with two segmented (i.e., piecewise) linear relationships separated by a break point (obtained from an iterative process described in Supplementary Material) highlighted by the filled black dot. The respective trend values are shown in the bottom part of the panel.

millions of hectares of wheat production were affected³⁶. In Paraguay, Uruguay and Southern Brazil, huge agricultural losses in maize, wheat and soybean production were also recorded and many Brazilian farmers were forced to request economic assistance³⁶. Alongside, extremely low levels in discharge in both Paraná and Paraguay rivers were observed, leading to serious constraints in the hydropower generation and water supply, and to the interruption of waterways that are essential for the fluvial transport and economy of these countries^{36,37}. This prolonged and intense drought also affected, particularly during 2020, the Pantanal biome, which is the largest contiguous wetland on the planet and home to a large variety of animal and plant species³⁸. Pronounced soil dry-out in the region coincided with several heatwaves, leading to periods characterized by a rapid and sudden intensification of the drought conditions and a large evaporative stress^{17,39}. This short-term (weekly to monthly) periods, marked by a rapid rate of intensification of the already established dry conditions, are usually referred as flash droughts and are often linked to more severe impacts than the slowly evolving droughts⁴⁰. In Pantanal, these flash droughts raised fire danger to levels not seen since 1980 and led to devastating fires³⁹, resulting in one-third of the biome burnt and economic losses of

around USD 3.6 billion³⁹. The extreme drought lasted until the end of 2022, spreading from Pantanal to wider areas in CESA⁴¹.

This study seeks to provide a detailed spatiotemporal characterization of the unprecedented 2019–2022 drought in CESA, exploring the historical context of the event, assessing the exceptionality of the soil moisture anomalies and describing the atmospheric mechanisms involved from a daily to multiyear timescale perspective. Overall, we aim to contribute to a better understanding of the dynamical processes associated with internal variability, and thus to improve the predictability of climate extremes in future.

RESULTS

The 2019–2022 drought in a historical context

Most of SA has been witnessing, particularly after the 1990's decade, a significant land surface drying trend, with CESA (limited by the red box show in Fig. 1a), revealing the steepest soil moisture decrease, particularly over the Pantanal, Southeast Brazil, central Paraguay and northern Argentina (Fig. 1a). When analyzing long-term changes in climate for CESA (Fig. 1b and Supplementary Fig. 1), a pronounced shift towards higher temperatures from the first half of the analysis period (1959–1989) into the second half

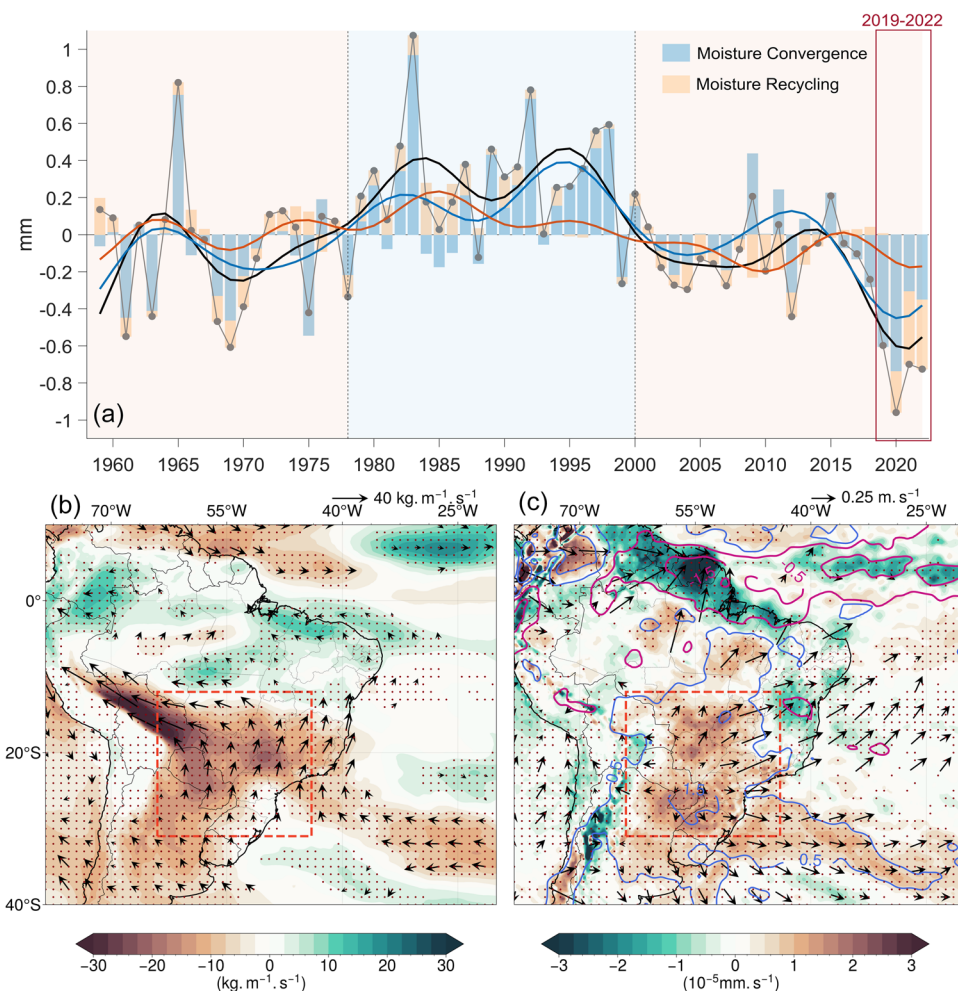


Fig. 2 Long-term inter-annual variability of moisture convergence and precipitation over CESA. **a** Time series of mean annual anomalies over CESA of daily accumulated precipitation (gray line, mm), and daily accumulated precipitation due to vertically integrated moisture convergence (blue bars, mm) and due to moisture recycling (orange bars, mm). The bold lines depict the respective time series filtered by a 10-year low pass Lanczos filter. Light orange and blue background colors highlight decadal periods defined by drier and wetter condition, respectively. **b** Anomaly composites (regarding the 1981–2010 climatology) of IVT obtained considering the mean observed conditions during the 2019–2022 drought period (color shading, $\text{kg.m}^{-1}\text{s}^{-1}$), and direction (vector – only the statistically significant anomalies at a 5% level are shown according to the Student's two-tailed t test). **c** Anomaly composites for the 2019–2022 period of the vertical integral of divergence of moisture flux (color shading, mm.s^{-1}) and of the divergent wind field at the 850hPa level (vectors, m.s^{-1}). Blue and magenta contours delimitate regions covered by positive and negative anomalies of the daily evaporation minus precipitation balance, respectively. Red dots in **b** and **c** mark the statistically significant anomalies at a 5% level according to the Student's two-tailed t test.

(1990–2022) is observed – see blue and orange ellipses in Fig. 1b. Regarding precipitation, there is a less pronounced contrast in the distribution between both periods. However, a skewed distribution is observed during the second half of the period, indicating a few periods characterized by extreme low and high precipitation levels during recent decades. The correlation between precipitation and temperature is stronger for the second half ($R = -0.63$) than for the first half ($R = -0.43$), indicating that during the last three decades, dry years were more often associated with extremely warm conditions. This recent warmer and drier conditions explain a continuous decrease in soil moisture levels (Fig. 1c), particularly after 1990's decade (-0.010 per decade, statistically significant at a 5% level according to the Mann–Kendall two-tailed test), paving the way for the outstanding 2019–2022 drought. In fact, this 4-year period finds no parallel with any other period in the historical record, being unprecedented in terms of dryness intensity and duration.

When analyzing the total precipitation anomalies (gray and black lines in Fig. 2a) as well as the precipitation anomalies caused

only by the vertically integrated moisture convergence (VMC) (blue bars and line in Fig. 2a) in CESA for the 1959–2022 historical period, one can observe that they were characterized by a marked decadal variability and by the occurrence of a drier period during the first and last two decades and a wetter period during the 1980's and 1990's. The two variables present a Spearman's correlation coefficient of 0.92 over the entire period, statistically significant at a 5% level, showing that long-term disturbances in moisture convergence in CESA are strongly reflected in the total amount of precipitation in the region. On the other hand, moisture recycling seems to be less important in explaining inter-annual changes of precipitation anomalies as it shows a less pronounced decadal variability and a lower correlation coefficient ($R = 0.62$, statistically significant at a 5% level). The precipitation anomalies caused by moisture recycling show a decreasing trend after the 1980's (statistically significant at the 5% level), which likely results from the previously observed progressive reduction in soil moisture in the region (see Fig. 1c). In particular, the drought years of 2019 and 2020 experienced the two lowest ever recorded

VIMC levels, while 2021 and 2022 observed the two lowest contributions of moisture recycling for total precipitation.

The boxplots shown in Supplementary Fig. 2 highlight the statistical distribution of the mean annual values of daily vertically integrated water vapor transport (IVT) across each one of the four CESA borders depicted in Fig. 1a, with positive (negative) values indicating moisture inflow (outflow) to (from) CESA. The inflow of moisture occurs mostly throughout the northern and western borders while the outflow occurs mainly throughout the eastern and southern borders. The 2019–2022 drought years were defined by a lower than normal northern and western moisture inflow, which clearly contrasts with the higher-than-normal moisture inflow throughout these two limits during the four wettest years (1965, 1983, 1992 and 1998, see Supplementary Fig. 2). In fact, the correlation coefficients for 1959–2022 between the mean annual IVT over each one of the four frontiers and the mean annual VIMC over CESA (inset table in Supplementary Fig. 2), are positive and statistically significant at a 5% level for the northern ($R = 0.70$) and western borders ($R = 0.55$), indicating that the moisture convergence and precipitation anomalies are mostly determined by the amount of moisture inflow from Amazon. In contrast, the amount of moisture outflow through the eastern and southern borders does not play a significant role in moisture convergence in CESA. These results are corroborated when analyzing from a spatial perspective the anomalous IVT over SA, which shows an anomalous southeast–northwest orientation pattern during the 2019–2022 drought period (Fig. 2b), and an anomalous northwest–southeast orientation during the four wettest years (Supplementary Fig. 3a). Comparing with climatological conditions (see Supplementary Fig. 4), the IVT configuration observed during the 2019–2022 period points to a weakening of the expected northwest–southeast moisture transport from the Amazon basin towards CESA that is mostly supported by the SALL⁴².

Precipitation anomalies are determined not only by moisture availability but also by convergence patterns in the atmosphere. Accordingly, the positive anomalies of the vertical integral of divergence of moisture flux in CESA, reveal that during the 2019–2022 drought the region was characterized by a lower-than-normal moisture convergence (Fig. 2c). The anomalous low tropospheric (850hPa) wind field shows enhanced divergence and air spread from CESA towards the surrounding regions, highlighting pronounced subsidence and clear sky conditions. These conditions were responsible for large precipitation deficits in CESA and thus for positive anomalies in evaporation minus precipitation (E-P) in the region (see blue contours in Fig. 2c). Moreover, this divergence implied anomalous advection from CESA towards north SA, where pronounced moisture convergence and negative anomalies in E-P prevailed. The mean observed conditions during the wettest years show a clear contrasting pattern (Supplementary Fig. 3b). The regression maps shown in Figure S5 support this relationship, indicating that throughout the 1959–2022 period, increasing IVT and decreasing levels of the vertically integrated divergence over CESA were associated with enhanced local precipitation.

A closer insight into the 2019–2022 drought: evolution, exceptionality and spatial extent

The time series for the 2019–2022 period of the R-index, a metric defined to rank extreme and widespread drought events using soil moisture anomalies (see “Methods section”), presents a relatively large variability resulting from pronounced fluctuations of both the drought intensity and spatial extent. At the beginning of 2019, marked dry conditions started to affect CESA (Fig. 3a). The R-index peaks for the first time on January 26th (9th and 36th in the ranking classification considering the short 2019–2022 and the long 1951–2022 periods, respectively), highlighting a rapid and pronounced soil desiccation and the occurrence of a flash drought

over southeast Brazil and the Pantanal biome (see left panel of Fig. 3c). Analyzing Fig. 3b and the color shading level intercepted by the purple line which depicts the 31-day time scale (the time scale used to obtain the running mean filtered soil moisture anomalies that were input for the R-index), one can observe that this period was characterized by several areas within CESA experiencing record-breaking low soil moisture levels (with a total extension of around 100 000 km²). Later, during the following months, there was a clear amelioration of the drought, with R-index reaching values closer to zero. However, the year 2020 witnessed the most critical conditions with the occurrence of several flash drought episodes, particularly during the months of March, April, October, November and December, when many regions in CESA experienced a record-breaking soil dry-out (Fig. 3b). In fact, the five most severe R-index peaks occurred within each of these particular months, with April 26th (peak #1) witnessing the lowest R-index on record (since 1951). More than 30% of CESA experienced soil moisture anomalies larger than two standard deviations on that day (see purple shaded area in Fig. 3a) and a total area of around 100 000 km² was affected by record-breaking drying conditions (Fig. 3b). When considering longer temporal scales (seasonal and annual), the amount of CESA covered by unprecedented low soil moisture increases, underlying the exceptional duration of the event. For instance, for temporal scales between 300 and 365 days, more than 700 000 km² (20% of the total area of CESA) witnessed record-breaking soil dryness. Moreover, the spatial signature of the drought throughout 2020 was considerably variable (Fig. 3c). Marked dry conditions started to be recorded in March over Pantanal and southern Brazil (see the turquoise shading in the second panel of Fig. 3c, associated with peak #4). Later, during April, the drought signal expanded south and eastwards, towards south Brazil, north Argentina and central Paraguay as shown by the red color shadings associated with peak #1 in the middle panel of Fig. 3c. In October and during the flash drought marked by the peak #5 (October 10th), the soil dry-out pattern moved slightly northwards affecting more the central CESA. During the last two months of 2020, when peak #3 and #2 occurred, soil dryness dominated over the northern section of CESA and Pantanal. Later, the year of 2021 started with a slight weakening of the drought signal (Fig. 3a), however a strong amplification occurred in April with pronounced soil desiccation being recorded over Pantanal (red area in the third panel of Fig. 3c). Finally, the year of 2022 witnessed a new intensification of the pre-established drought conditions, mainly during the 1st half of the year and the final months of November and December. The right panel in Fig. 3c highlights that, once again, Pantanal and the northward surrounding region were the most affected areas in CESA during the occurrence of the two most extreme flash drought events recorded in 2022 (peak #6 and #7).

The influence of large-scale tropical and subtropical atmospheric forcing on the 2019–2022 drought

Decadal-scale variability such as the one observed when analyzing the long-term inter-annual variability of precipitation and VIMC over CESA (Fig. 2a), is often associated with slowly varying atmospheric and/or oceanic conditions (e.g., sea surface temperature, atmospheric pressure^{31,33,43}) described by a particular large-scale atmospheric-oceanic variability mode. Figure 4a provides the spatial correlation between the mean annual SST's and the mean annual IVT across the northern border of CESA, which controls the amount of moisture convergence and precipitation in the region. The central and southeast tropical Pacific reveal pronounced positive and statistically significant correlations, indicating that mean annual wet conditions over CESA are associated with warmer SSTs in these areas of the Pacific Ocean and with ENSO. Statistically significant negative correlations were also observed over the equatorial Atlantic Ocean, as well as over the southwest

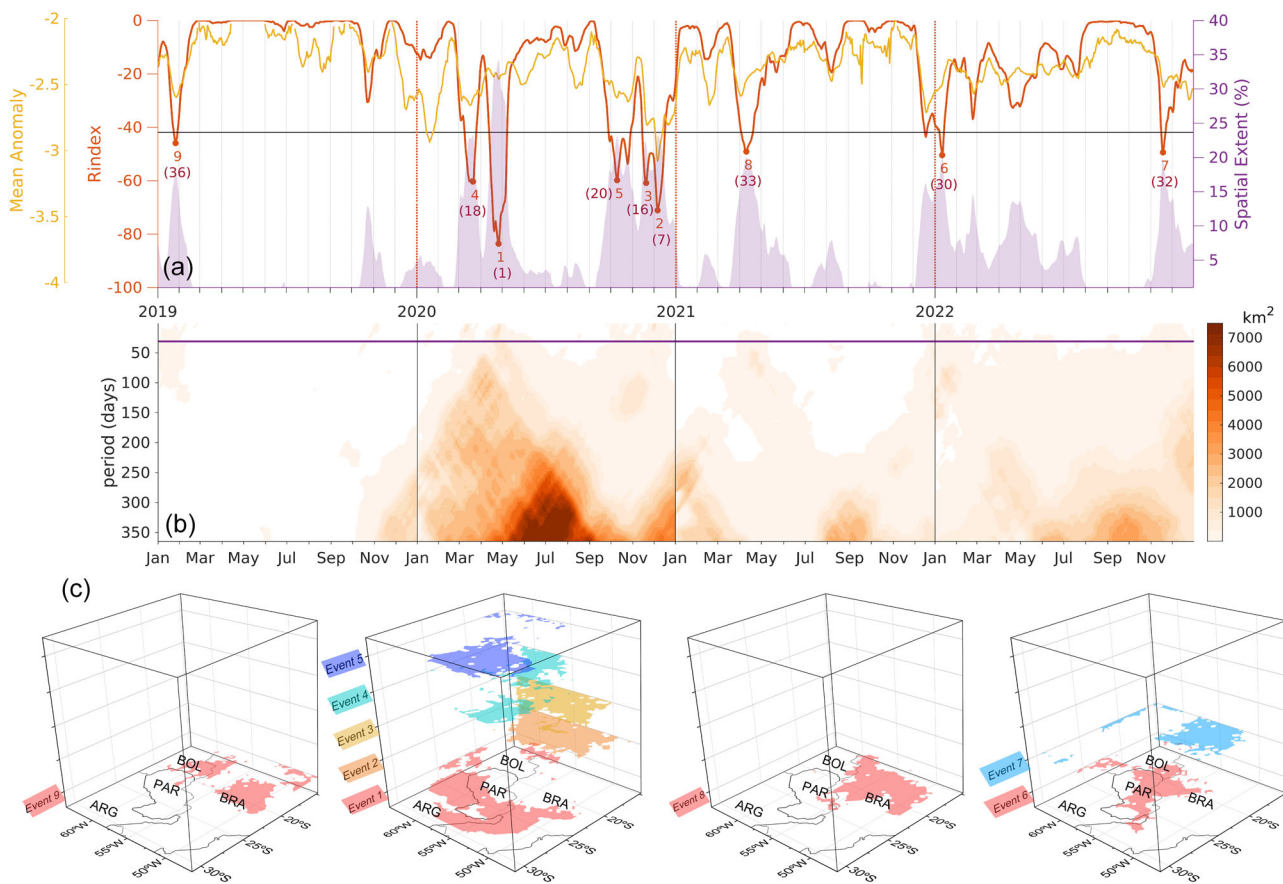


Fig. 3 The 2019–2022 drought from a daily perspective: exceptionality and spatial extend. **a** Time series of the R-index (red line, left y-axis) and of the two sub-indexes: mean anomaly (yellow line, left y-axis) and spatial extent (lilac shade, right y-axis) for the 2019–2022 drought in CESA (for more information see the “Methods” section). The black line depicts the 2.5th percentile of the R-index considering all the analysis period from ERA5-land dataset (1951–2022). The red filled dots identify the nine most extreme peaks of low R-index levels observed during the 4-yr period. The red numbers rank the peaks according to their intensity. The ones out of brackets show the rankings only considering the R-index levels obtained during the 4-year drought period, while the numbers inside brackets consider the R-index levels for all the analysis period. **b** Daily temporal evolution of the spatial extend (in 10^2 km^2) of areas within CESA experiencing record-breaking low soil moisture anomalies, computed for several time-scales by applying a running mean filter with time windows between 1-day and 365-day. **c** Three-dimensional framework showing the location of the grid-points within CESA that observed daily negative soil moisture anomalies higher than two standard deviations during each of the nine extreme peaks of the R-index.

and northwest Pacific, pointing for a potential link between CESA moisture conditions and the Pacific Decadal Oscillation (PDO). When analyzing the decadal variability of the Southern Oscillation Index (SOI) and of Oceanic Niño Index (ONI) (see Supplementary Material), we observe that multi-year dry periods in CESA were defined by positive values of SOI and negative levels of ONI, thus to La Niña conditions (Fig. 4b). Moreover, a lead-lag relationship between these time series seems to be present. The correlation between these ENSO indicators and the IVT across the northern border of CESA, was high and statistically significant during the autumn, winter and spring seasons, while during summer, residual and non-statistically significant correlations were obtained (see inset table in Fig. 4). From an annual perspective and filtering all signals with a 10-yr low pass filter, correlations reach higher levels than the ones obtained considering the non-filtered time series (see Fig. 4 inset table). The same is observed with PDO (table S1). This points for a stronger link between CESA precipitation and all these Modes of variability when considering long-term decadal oscillations. Regarding the Atlantic Ocean, the variability of precipitation levels in CESA appears to be negatively correlated with the Atlantic Zonal Mode (AZM), although this relation is, in general, less pronounced compared to the other two modes of variability in Pacific.

The spatial distribution of the observed SST anomalies during the 2019–2022 drought period shows cold SSTs in tropical central and southeast Pacific associated to enhanced low tropospheric air divergence (Fig. 5). Such anomalous divergence pattern (see vectors in the lower panel of Fig. 5) is a signature of above-normal subsidence as shown by the positive anomalies of the vertical velocity over central tropical Pacific and northwest SA (middle panel in Fig. 5). The subsidence over northwest SA represents the descending branch of an eastward shifted Walker Cell (descending blue arrow in Fig. 5), strongly connected to anomalous convergence at the top of the atmosphere, as shown by the positive anomalies of velocity potential (Fig. 5, top panel). The corresponding ascending branch, linked with divergence at the top of the atmosphere and convection, was located in the equatorial Atlantic near northeast SA (see ascending blue arrow in Fig. 5), supporting the low tropospheric moisture convergence patterns and the negative anomalies of E-P balance that were previously identified for this region (see Fig. 2d). Moreover, Fig. 5 shows that this large-scale anomalous zonal circulation was strongly connected with subtropical SA, through the establishment of an amplified meridional Hadley Cell (see purple lines in Fig. 5) with its descending branch associated with clear sky conditions, strong diabatic and adiabatic heating rates and

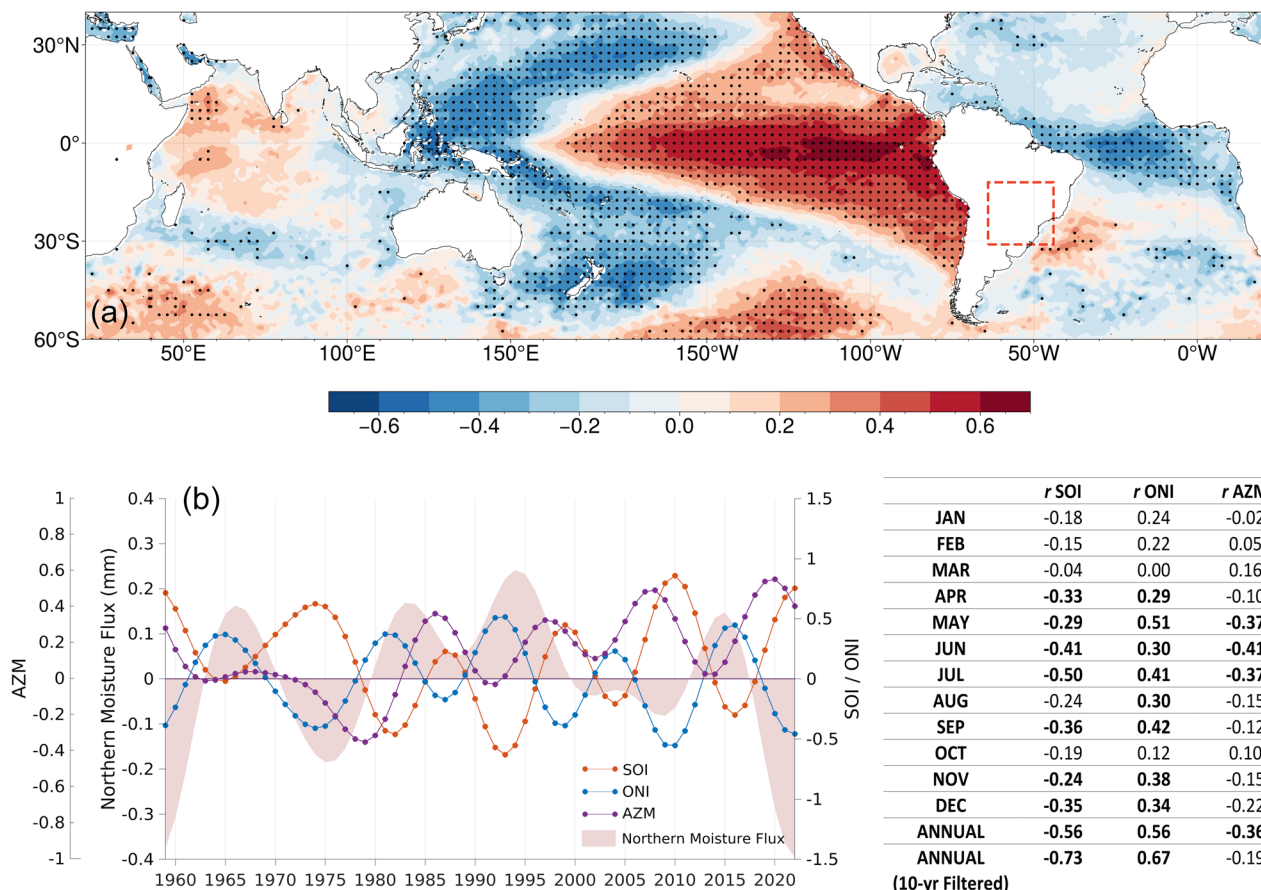


Fig. 4 The impact of large scale atmospheric-oceanic modes of variability in CESA moisture inflow. **a** Spatial distribution of Spearman's correlation coefficients between the mean annual SST and the IVT across the northern border of CESA obtained for the 1959–2022 period. **b** Time series from 1959 to 2022 of the mean annual anomaly levels of daily IVT across the northern border of CESA (shaded area; left y-axis), of the Atlantic Zonal Mode (purple line; left y-axis), the Southern Oscillation Index (orange line; right y-axis) and the Oceanic Niño index (blue line; right y-axis) filtered by a 10-year low pass Lanczos filter. The inset right table highlights the annual and monthly Spearman's correlation coefficients obtained between the non-filtered time series of three indexes and the northern moisture transport over CESA for the 1959–2022 period. The last row shows the correlations obtained considering the times series filtered by a 10-year low pass Lanczos filter. In bold are shown the statistically significant correlation coefficients at a 5% significant level according to the Student's two-tailed *t* test.

moisture divergence, located over CESA. Accordingly, this descending branch promoted the low tropospheric spread of large amounts of moisture from CESA towards the surrounding regions and particularly towards northeast SA, where it converged, explaining the positive anomalies of the E-P balance that were previously identified in Fig. 2d. The three wettest years were characterized by a contrasting tropical zonal and meridional circulation, with the establishment over CESA of a Hadley cell's ascending branch associated with strong moisture convergence and supply from the Amazon basin (Supplementary Fig. 6).

In addition to this anomalous tropical circulation responsible for the long-term precipitation deficits in CESA during the 2019–2022 drought, at synoptic scales, the subtropical dynamic may also have played a key role in explaining the occurrence of the flash droughts identified by the R-index peaks. Accordingly, we computed spatial anomaly composites considering the nine most extreme R-index peaks (Fig. 3a) and regarding several meteorological parameters (Fig. 6). Pronounced negative soil moisture anomalies are clearly visible all over CESA (Fig. 6a). The mid-level atmospheric circulation was defined by the occurrence of positive 500hPa geopotential height anomalies and by exceptional warm conditions in the low troposphere, likely promoted by strong air subsidence, enhanced adiabatic and diabatic heating rates (Fig. 6b). The occurrence of positive anomalies of the vertical integral of

divergence of moisture flux (see color shading in Fig. 6c) and the spreading out of air masses from CESA to the surrounding regions, as indicated by the anomalous low tropospheric divergent wind field (see arrows in Fig. 6c), is evident. This points to the establishment over CESA of exceptional clear-sky conditions and strong shortwave radiation incidence at the surface that led to large evaporation rates. From a large-scale perspective and in agreement with Fig. 5, it is possible to observe the establishment of a meridional Hadley cell (Fig. 6d) with enhanced divergence at the top of the atmosphere over northeast SA (see the negative anomalies of potential velocity represented by the color shading in Fig. 6d), and its descending branch over CESA. Regarding the mid-latitude atmospheric circulation, the anomalous meridional wind field at the 200 hPa level shows a clear sequence of divergence/convergence patterns in the top of the troposphere spanning from west-central south Pacific to south Atlantic (Fig. 6e). This is a clear signature of a Rossby wave train (wavenumber 3) embedded in a jet stream that experienced an anomalous poleward shift over southeast South Pacific, near SA (see contours in Fig. 6e)⁴⁴. A large Rossby wave source region was recorded in west-central Pacific, at east and south Australia, where the Rossby wave train was formed (Fig. 6f). At east of Australia, the Rossby wave forcing was mostly due to the advection of absolute vorticity by the divergent flow (see Supplementary Fig. 7a) and to strong

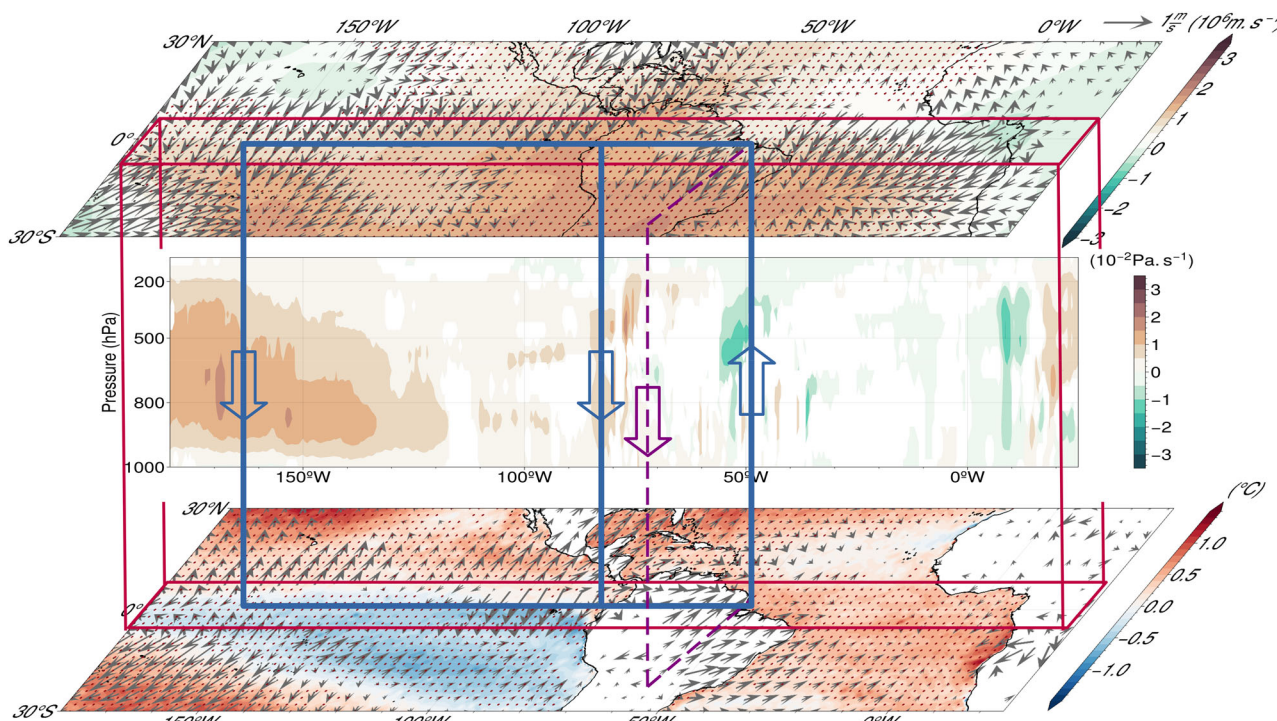


Fig. 5 Large-scale tropical dynamics associated with dry conditions in CESA. Three-dimensional schematic framework of the oceanic and atmospheric mean anomalous conditions observed during the 2019–2022 drought. The lower panel highlights the SST anomalies (color shading, $^{\circ}\text{C}$) and the mean anomalous pattern of the low-tropospheric (850hPa) divergent wind field (vectors, m.s^{-1}). The middle panel shows a zonal-vertical circulation in a latitudinal band between 5°N and 5°S , with the color shading depicting the mean anomalies in vertical wind velocity (10^{-2}Pa.s^{-1}). Only the statistically significant anomalies (p value < 0.05) are shown according to the Student's two-tailed t test. The top panel illustrates the mean anomalous field of velocity potential (color shading, 10^6m.s^{-1}) and of the 200hPa divergent wind (vectors, m.s^{-1}). The anomalies were filtered using a 31-day running mean filter. Red dots and vectors shown in the top and bottom panels mark the statistically significant anomalies at a 5% level, according to the Student's two-tailed t test.

convection in the Indo-Pacific warm pool, while at south of Australia only dynamic factors were involved (Supplementary Fig. 7b) which agrees with Shimizu et al.⁴⁵. Finally, from a long-term perspective, this 4-yr drought was characterized by a clear zonal expansion of the subtropical quasi-stationary high-pressure system in the south Atlantic, with a higher-than-normal continental penetration towards SA when compared to the mean climatology. This points for a higher influence of this system in modulating precipitation deficits mainly in the eastern section of CESA (Supplementary Fig. 8). A similar zonal expansion of the south Pacific high-pressure system was observed, leading to pronounced positive mean sea level pressure anomalies in South Pacific, over 150°W and 100°W , in a latitudinal band between 35°S and 45°S (see color shading in Supplementary Fig. 8). This suggests an increased ridging activity in the region⁴⁶. Consequently, the mean position of the subtropical Southern Hemisphere jet stream suffered a poleward shift over southeast south Pacific, near SA, reducing the passage of cyclones and frontal systems over the southernmost regions of CESA.

DISCUSSION

Despite the outstanding amplitude and length of the 2019–2022 drought, it is paramount to stress that it occurred within the context of a prolonged drying trend observed over the past three decades in CESA, that resulted from a joint contribution of natural decadal variability in precipitation levels and increasing temperatures. The observed decadal variability in precipitation was found to be mainly controlled by ENSO, with La Niña events, such as the recent one extending from 2020 to 2022⁴⁷, being associated to

precipitation deficits over CESA. A lead-lag relationship between ENSO indicators and CESA precipitation appears to be present (Fig. 4b). However, there is a week consistency of the leading and lagging time series throughout the analysis period, which motivates further investigation for a better understanding. An association between PDO and precipitation in CESA was also found, particularly when considering decadal oscillations (Supplementary Table 1 and Supplementary Fig. 9). Previous studies have shown that PDO influences El Niño teleconnections over South America particularly during the warm season. According to Kayano and Andreoli⁴³, rainfall anomalies over SA are enhanced when a negative (positive) phase of the PDO concurs with La Niña (El Niño) conditions in a situation similar to the one during the 2019–2022 period (Supplementary Fig. 9). The observed negative SST anomalies in eastern tropical Pacific were found to promote large-scale disturbances in the location and intensity of the Walker cell modulating the southwards moisture transport from the Amazon and the water vapor convergence over SA. Disturbances in these two hydrological processes are reflected in the amount of precipitation over CESA^{27–29}. This agrees with previous studies that demonstrated an influence of La Niña conditions in precipitation over SA through a similar tropical pathway^{30,48}. Our study adds another layer to this known tropical teleconnection by showing how the anomalous Walker circulation could trigger a secondary meridional circulation and strong subsidence over CESA.

On the other hand, deforestation has been associated to less moisture of Amazonian origin and to precipitation reductions in non-deforested parts of the western Amazon and in regions further downstream, mainly CESA^{49,50}. Therefore, recent

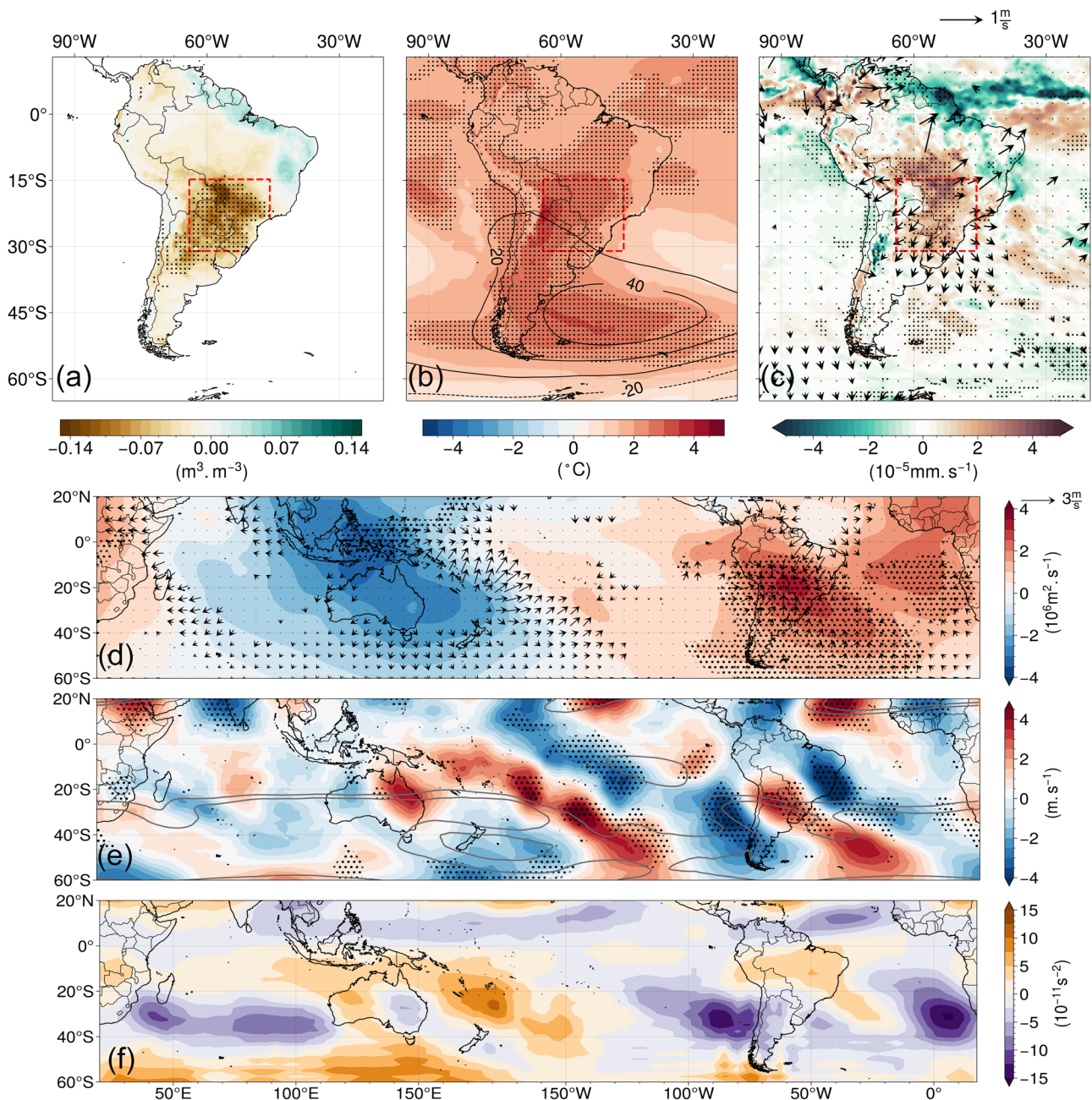


Fig. 6 Large-scale tropical-extratropical teleconnection during the 2019–2022 drought over CESA. Spatial distribution of composite anomalies and mean observed values during the days that recorded the nine lowest R-index peaks (see Fig. 3a) of several land and meteorological parameters: **a** Anomalies of soil moisture (color shading, m^3/m^3); **b** Anomalies of the 500hPa geopotential height (contours, gpm) and of the 850hPa temperature (color shading, $^{\circ}\text{C}$); **c** Anomalies of the Vertical Integral of divergence of moisture flux (color shading, 10^{-5}mm.s^{-1}) and of the divergent wind field at the 850hPa level (vectors, m.s^{-1}); **d** Anomalies of the velocity potential (color shading, $10^6 \text{m}^2.\text{s}^{-1}$) and of divergent wind field at the 200hPa level (vector, m.s^{-1}); **e** Anomalies of the 200hPa meridional wind (color shading, m.s^{-1}). The gray solid lines show the mean observed 200hPa zonal wind pattern (contour levels: 25, 35, 45 m.s^{-1}). **f** Rossby wave source (color shading, 10^{-11}s^{-2}). The anomalies and the mean observed values were filtered using a 31-day running mean filter. Black dots and vectors highlight the respective statistically significant anomalies at a 5% level according to the student's two-tailed t test.

deforestation may have enhanced the impact of La Niña on precipitation deficits over the last two decades in CESA, paving the way for the outstanding 2019–2022 drought. Soil moisture anomalies during this 4-yr period were defined by a large spatiotemporal variability. Flash droughts in 2020 affected multiple regions such as Pantanal, Bolivia, Paraguay and North Argentina, and led to large areas covered by record-breaking soil moisture anomalies ($\sim 100.000 \text{km}^2$) and warm temperatures fueled

by strong soil moisture–temperature coupling³⁹. Such severe drought conditions can cause devastating losses in agriculture and livestock production, depletion of water resources, reduction of air quality and exacerbated wildfire risk^{51,52}. The Pantanal's catastrophic wildfires recorded during the spring months of October and November 2020 clearly expose this link^{38,39}. In fact, the most severe drought conditions, associated with record-breaking soil desiccation, were observed during autumn and

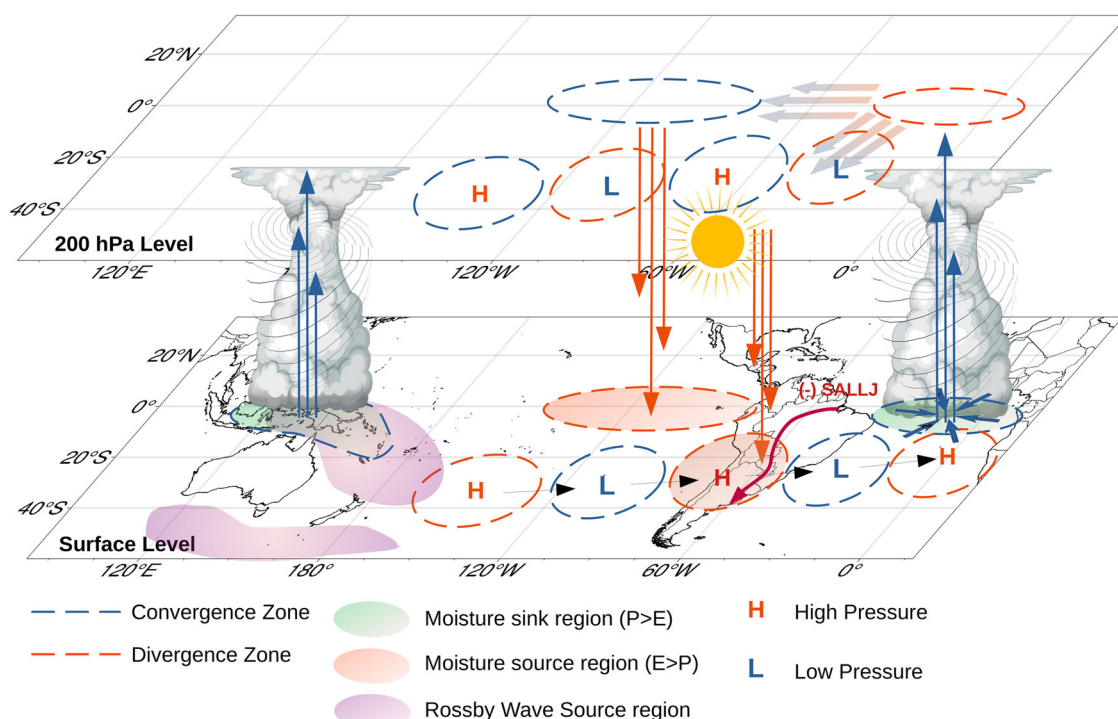


Fig. 7 Large-scale atmospheric dynamics responsible for the 2019–2022 drought. Conceptual model showing in an illustrative and schematic framework the coupled tropical and subtropical atmospheric forcing responsible for the 2019–2022 drought and for the record-breaking soil desiccation.

spring in 2019–2022 (Fig. 3a), hence during the months before and after winter, when climatological soil water content in CESA reaches the lower levels (Supplementary Fig. 10).

To summarize the tropical and mid-latitude mechanisms mentioned in the previous sections we propose a conceptual scheme (Fig. 7) that aims to capture the coupled large-scale tropical and subtropical atmospheric dynamics responsible for the historically unprecedented soil desiccation in CESA during the 2019–2022 drought. Enhanced surface air convergence over northeast SA and tropical Atlantic Ocean, linked to negative SST anomalies in tropical Pacific and to an anomalous ascending branch of an eastward shifted Walker Cell, was responsible for precipitation deficits and large evaporation rates in CESA via two distinct processes. First, enhanced deep convection in northern Brazil and equatorial Atlantic led to a decrease in this region of moisture available to be advected and a weakening of the northeast trade winds, causing a reduction of the SALLJ activity⁴². Secondly, this eastward shifted Walker Cell induced a meridional Hadley cell and enhanced subsidence over CESA, resulting in the suppression of moisture convergence and precipitation. The SALLJ is defined as a low tropospheric northerly jet along the eastern slopes of the Andes responsible for the transport of large amounts of moisture from the Amazon to the subtropics^{42,53,54}. In agreement with our results, previous studies have shown that at interannual timescales, this jet is strongly modulated by ENSO, and La Niña conditions are associated with weaker and less frequent jet days^{29,53}. Here we demonstrated that negative precipitation anomalies in CESA were also found to be related to AZM and so to positive SST anomalies in tropical Atlantic. Although we did not explore in detail this association, our results corroborate Barreiro and Tippmann⁵⁵ showing that positive phases of the AZM induce equatorial westerlies, leading to a weakening of the SALLJ activity and therefore to long-term precipitation deficits over CESA. During the flash drought episodes, when soil desiccation reached its maximum intensity and spatial extent, a Rossby wave pattern, reinforced the subsidence over CESA and the already

established descending branch of the meridional Hadley Cell. This compound mechanism connecting the tropical and subtropical anomalous dynamics resulted in the establishment over CESA of a quasi-stationary anticyclonic circulation known to enhance evaporation and reduce soil moisture levels¹⁷. This Rossby wave train was forced at east and south of Australia in regions known to bring together the ideal conditions for the development of such atmospheric patterns^{34,45,56,57}. These Rossby wave source regions were closely linked to strong convection in the western tropical Pacific and to local warm SST's, typically associated with La Niña episodes (Fig. 7). Our results support previous works that had shown the capability of ENSO to modulate precipitation over CESA through such an extratropical pathway, known as the Pacific–South American pattern^{30,57,58}. Particular phases of the MJO were also linked to these Rossby Wave trains and so to warm and dry extremes in SA^{32,56}. MJO and ENSO are both influenced by SST anomalies in the western Pacific although both modes are defined by distinct times scales. ENSO, as a key slowly-varying “external” forcing, regulates the background mean state (i.e., the lower-tropospheric winds and humidity) capable to modulate MJO, which is the dominant mode of tropical intraseasonal variability on which these weekly to monthly Rossby Wave Patterns express their main temporal signature^{59,60}. Moreover, the trajectory of these extratropical wave structures as well as the passage of transient systems particularly over the southernmost regions of CESA is influenced by the southern Hemisphere westerlies and by the subtropical jet stream. Although no relevant correlations were obtained between the Southern Annular Mode and the tropical moisture inflow towards CESA (table S1), this mode of variability in the Southern Hemisphere might influence the westerlies and the positioning and intensity of the subtropical jet stream current, leading to precipitation changes in the more extratropical areas of CESA⁶¹. In this context, we have shown that during 2019–2022 there was a clear zonal expansion of the South Pacific high-pressure system associated to a poleward shift of the jet stream (Supplementary Fig. 8). A similar change in the

trajectory of the jet stream has been associated to positive SAM phases such as the one that has been characterizing the last two decades (Supplementary Fig. 9)^{61,62}.

The findings, summarized in a conceptual model in Fig. 7, highlight the effect of internal variability in the occurrence of climate extremes, providing a guideline to characterize other historical drought events and to predict the occurrence of future extreme dry spells together with climate models capable to simulate such dynamical processes in tropical and subtropical regions. Moreover, previous studies have identified CESA as a region with strong soil moisture–temperature and soil moisture–precipitation feedbacks^{63,64}. In fact, recent hot extremes (e.g., 2020 in Pantanal and 2013/2014 in Southeast Brazil) resulted from a joint contribution of large-scale atmospheric circulation anomalies and a strong soil moisture imbalance^{17,39}. Libonati et al.³⁹ demonstrated how CESA was affected during 2020 by a strong soil moisture–temperature coupling regime and how the co-occurring conditions of pronounced soil desiccation and shortwave radiation incidence led to an increase of the sensible heat flux between surface and atmosphere. An amplification of temperature extremes and of the drought conditions, initially triggered by the atmospheric dynamics highlighted here, resulted in exceptional flammability conditions. However, it is important to stress that Libonati et al.³⁹ only explored a particular section of the total area in SA affected by the 2019–2022 drought (i.e., Pantanal). Therefore, further studies employing an extended spatial analysis and addressing more closely the link between the multiple atmospheric forcing mechanisms shown here and the amplification of the drought conditions through these land–atmosphere feedbacks, appear necessary.

Future climate change projections regarding land–atmosphere interactions in regions such as CESA, where soil moisture is a driving factor, are shrouded in large uncertainty^{64,65}. Recent studies suggest that CESA will remain a land–atmosphere coupling hotspot, with some regions (namely the Pantanal and Brazilian Highlands) witnessing a change from energy-limited to water-limited regimes, and a higher concurrence of dry and hot spells^{66,67}. Moreover, these results highlight how internal variability represents a key factor for the occurrence of long-term dry and wet periods in SA, stressing the need of climate models to better simulate the atmospheric dynamics associated to this climate variability. This is particularly relevant when considering precipitation projections at a local scale for which internal climate variability is the dominant source of uncertainty^{68,69}. Some studies have shown disparities between state-of-the-art climate models and observations regarding the effect of global warming in the tropical Pacific dynamics and particularly in the Walker Circulation^{70,71}. This points for a critical failure of models to correctly modulate key features of ENSO and other atmospheric dynamics linked to climate variability that, as we have shown here, influences long-term changes in precipitation and evaporation in South America, putting into question the known projections of these variables for the continent. Accordingly, this study provides robust guidelines to better predict the occurrence of future dry extremes, stressing the urgent need to improve the representation of the dynamical processes associated with daily-to-multiyear timescales in climate models. We believe these findings will be of interest to the international community in the context of natural hazards characterization and prediction under a climate change scenario.

METHODS

Data

Daily data from several meteorological parameters at surface and at different pressure levels, such as precipitation, temperature, specific humidity, zonal and meridional wind, geopotential and vertical velocity were extracted from the European Centre of

Medium-range Weather Forecast ERA-5 reanalysis datasets (Copernicus Climate Change Service, C2S, 2017) for the 1959–2022 period⁷⁰. Daily soil moisture levels (0 – 7 cm soil depth) for the 1951–2022 period were obtained from the ERA5-Land reanalysis which replaced the land component of the ERA5 model providing a better representation of the hydrological cycle⁷¹. ERA5-Land shows a good performance in estimating soil moisture levels when compared to other datasets, including satellite products and other models with and without data assimilation⁷². ERA5-Land soil moisture data is obtained using meteorological fields, such as precipitation and temperature, given by ERA5 that has incorporated a data assimilation scheme⁷³. ERA5 and ERA5-Land show for CESA smaller biases in precipitation than other known reanalysis such as JRA-55 and MERRA-2⁷⁴. The same is observed regarding the performance of ERA5 in estimating temperature extremes and the persistence of hot days^{75,76}. Although ERA5-Land, as a reanalysis product, has some disparities regarding observations, it provides the most reliable dataset for analysis of this kind on very long time periods and over wide regions such as SA and particularly CESA, where observations for variables such as soil moisture are unavailable⁷⁷.

Bivariate Gaussian Distributions

In order to estimate temperature–precipitation distributions for the two halves of the total period of analysis (1959–2022) and thus assess long-term changes in the bivariate distribution of these variables, two probability density functions assuming a bivariate gaussian distribution were computed for pairs of mean annual temperature and precipitation averaged over the red box in Fig. 1 (CESA) and during the periods of 1959–1989 and 1990–2022. Similarly to Bevacqua et al.⁷⁸, we assume that a bivariate Gaussian distribution is acceptable for mean annual values of these two variables allowing for a simple understanding of their compound effect on soil moisture levels, with the hypothesis that in some particular grid-points both precipitation and temperature datasets may have a skewed (Gamma) distribution.

The Vertically Integrated Water Vapor Transport

The vertically integrated water vapor transport (IVT) quantifies the total horizontal moisture transport by integrating over the vertical column of the atmosphere the zonal (Q_λ) and meridional (Q_ϕ) transport of specific humidity, defined as follows⁷⁹:

$$\text{IVT} = \left[\left(\frac{1}{g} \int_{\text{SURF}}^{\text{TOA}} qudp \right)^2 + \left(\frac{1}{g} \int_{\text{SURF}}^{\text{TOA}} qvdp \right)^2 \right]^{\frac{1}{2}} \quad (1)$$

with,

$$Q_\lambda = \frac{1}{g} \int_{\text{SURF}}^{\text{TOA}} qudp \quad (2)$$

$$Q_\phi = \frac{1}{g} \int_{\text{SURF}}^{\text{TOA}} qvdp \quad (3)$$

where q is the specific humidity, u and v are the zonal and meridional components of wind, respectively, g is the gravitational acceleration and dp an infinitesimal element of vertical pressure.

Considering this definition for the meridional and zonal components of the IVT, the vertically integrated moisture divergence can be computed using finite differences as follows:

$$\nabla \cdot \vec{Q} = \frac{\partial Q_\lambda}{\partial x} + \frac{\partial Q_\phi}{\partial y} \quad (4)$$

Accordingly, when the divergence is positive (negative) the atmospheric circulation is acting to decrease (increase) the water vapor transport over all the column of the atmosphere.

The Water Vapor Balance Over CESA

According to previous studies^{79,80} the total (net) vertically integrated moisture convergence (VIMC) over CESA, whose area is geographically defined in Fig. 1 (see red box), can be obtained as a line integral that accounts for the IVT across the western (F_w), the northern (F_N), the eastern (F_E) and the southern (F_S) borders:

$$VIMC = F_w + F_N + F_E + F_S \quad (5)$$

with,

$$F_w = \int_{\phi=31^{\circ}S}^{\phi=15^{\circ}S} Q_\lambda d\phi, \lambda = 64^{\circ}W \quad (6)$$

$$F_E = - \int_{\phi=31^{\circ}S}^{\phi=15^{\circ}S} Q_\lambda d\phi, \lambda = 44^{\circ}W \quad (7)$$

$$F_N = - \int_{\lambda=64^{\circ}W}^{\lambda=44^{\circ}W} Q_\phi d\lambda, \phi = 15^{\circ}S \quad (8)$$

$$F_S = \int_{\lambda=64^{\circ}W}^{\lambda=44^{\circ}W} Q_\phi d\lambda, \phi = 31^{\circ}S \quad (9)$$

Analyzing Eq. (9) and neglecting the water storage changes ($\frac{\partial w}{\partial t}$), when $VIMC > 0$, the region experiences a moisture flux convergence and acts as moisture sink if $P - E > 0$, or $E - P < 0$. On the other hand, when $VIMC < 0$, the region witnesses a moisture flux divergence and acts as moisture source if $P - E < 0$, or $E - P > 0$:

$$VIMC = P - E + \frac{\partial w}{\partial t} \quad (10)$$

The area-averaged precipitation rate due to moisture convergence ($P_{convergence}$) over CESA can be obtained dividing VIMC by the total area of the red box depicted in Fig. 1a:

$$P_{convergence} = \frac{VIMC}{A} \quad (11)$$

Accordingly, the contribution of moisture convergence to the total area averaged precipitation (P_{total}) can be computed by $\frac{P_{convergence}}{P_{total} \times 100}$, while the contribution of local moisture recycling due to evaporation can be obtained by:

$$100 \times \frac{(P_{total} - P_{convergence})}{P_{total}} \quad (12)$$

R-index: ranking soil moisture anomalies

The R-index is defined here as an adaptation of a metric initially proposed by Hart and Grumm⁸¹ and used in several studies^{82,83} to rank precipitation events on a daily basis. The exact same rationale was adopted here but considering soil moisture levels in CESA as input. First, daily standardized soil moisture anomalies regarding the seasonal climatology (1981–2010) were computed for each grid point within CESA and then filtered using a 31-day running mean filter. Thus, for each day of the analysis period (1951–2022) and for each grid-point within CESA we attained a normalized soil moisture departure value from the climatology. Ultimately, the R-index quantifies and ranks, on a daily basis, the magnitude of the soil moisture anomalies over CESA by multiplying (1) the area of CESA (in percentage) that experiences soil moisture anomalies lower than two standard deviations ("Spatial Extend") by (2) the mean soil moisture anomaly obtained by considering only the grid-points that recorded anomalies lower than two standard deviations ("Mean Anomaly").

Therefore, severe drought conditions are diagnosed when R-index reaches extremely low levels. Weekly to monthly peaks of this metric are linked to a sudden and rapid onset development of dry conditions and thus to flash drought episodes.

Rossby Wave Source

The Rossby Wave Source (RWS) was computed considering the barotropic vorticity equation in pressure coordinates^{84,85}:

$$RWS = -\zeta D - v_x \cdot \nabla \zeta \quad (13)$$

Where ζ is the absolute vorticity, obtained by summing the relative vorticity with the Coriolis parameter, and v_x is the non-rotational (i.e., divergent) wind vector component. The first term denotes the vortex stretching and accounts for the changing rate of vorticity, while the second term denotes the advection of vorticity by the divergent flow. Therefore, the Rossby Wave forcing tends to be higher in regions where divergence, divergent wind, absolute vorticity and the gradient of absolute vorticity is large. For instance, regions in the Western Pacific, at east and south of Australia, located on the edge of strong diabatic tropical heating and over the passage of the subtropical jet stream, where there are co-occurring conditions of high divergence, enhanced absolute vorticity and a high gradient of vorticity, reunite all the ideal conditions for a strong Rossby Wave forcing⁴⁵.

DATA AVAILABILITY

Data relevant to the analysis can be downloaded from the website listed below: ERA-5 and ERA5-Land reanalysis datasets are available at <https://cds.climate.copernicus.eu/cdsapp#!/search?type=dataset>. Data for the SOI, ONI, PDO, AZM and SAM indexes was provided by NCAR (National Center for Atmospheric Research) / Climate Data Guide, at <https://climatedataguide.ucar.edu/climate-data>. Datasets generated and analyzed during the current study are available from the corresponding author on reasonable request.

CODE AVAILABILITY

The code used in this study is available on request from the authors.

Received: 24 March 2023; Accepted: 24 October 2023;

Published online: 10 November 2023

REFERENCES

1. Chagas, V. B. P., Chaffé, P. L. B. & Blöschl, G. Climate and land management accelerate the Brazilian water cycle. *Nat. Commun.* **13**, 5136 (2022).
2. Donat, M. G., Lowry, A. L., Alexander, L. V., O'Gorman, P. A. & Maher, N. More extreme precipitation in the world's dry and wet regions. *Nat. Clim. Chang.* **6**, 508–513 (2016).
3. Wang, S.-Y. S., Yoon, J.-H., Becker, E. & Gillies, R. California from drought to deluge. *Nat. Clim. Chang.* **7**, 465–468 (2017).
4. Haddeland, I. et al. Global water resources affected by human interventions and climate change. *Proc. Natl. Acad. Sci.* **111**, 3251–3256 (2014).
5. Konapala, G., Mishra, A. K., Wada, Y. & Mann, M. E. Climate change will affect global water availability through compounding changes in seasonal precipitation and evaporation. *Nat. Commun.* **11**, 1–10 (2020).
6. Lesk, C., Rowhani, P. & Ramankutty, N. Influence of extreme weather disasters on global crop production. *Nature* **529**, 84–87 (2016).
7. Seddon, A. W. R., Macias-Fauria, M., Long, P. R., Benz, D. & Willis, K. J. Sensitivity of global terrestrial ecosystems to climate variability. *Nature* **531**, 229–232 (2016).
8. Kumar, S., Lawrence, D. M., Dirmeyer, P. A. & Sheffield, J. Less reliable water availability in the 21st century climate projections. *Earth's Futur.* **2**, 152–160 (2014).
9. Trenberth, K. E. Changes in precipitation with climate change. *Clim. Res.* **47**, 123–138 (2011).
10. Zhou, S. et al. Soil moisture–atmosphere feedbacks mitigate declining water availability in drylands. *Nat. Clim. Chang.* **11**, 38–44 (2021).
11. Dirmeyer, P. A., Wang, Z., Mbuh, M. J. & Norton, H. E. Intensified land surface control on boundary layer growth in a changing climate. *Geophys. Res. Lett.* **41**, 1290–1294 (2014).
12. Miralles, D. G. et al. Contribution of water-limited ecoregions to their own supply of rainfall. *Environ. Res. Lett.* **11**, 124007 (2016).
13. Jung, M. et al. Recent decline in the global land evapotranspiration trend due to limited moisture supply. *Nature* **467**, 951–954 (2010).

14. Miralles, D. G., Gentine, P., Seneviratne, S. I. & Teuling, A. J. Land-atmospheric feedbacks during droughts and heatwaves: state of the science and current challenges. *Ann. N. Y. Acad. Sci.* **1436**, 19–35 (2019).
15. Taylor, C. M. et al. Frequency of Sahelian storm initiation enhanced over mesoscale soil-moisture patterns. *Nat. Geosci.* **4**, 430–433 (2011).
16. Taylor, C. M., de Jeu, R. A. M., Guichard, F., Harris, P. P. & Dorigo, W. A. Afternoon rain more likely over drier soils. *Nature* **489**, 423–426 (2012).
17. Geirinhas, J. L. et al. The influence of soil dry-out on the record-breaking hot 2013/2014 summer in Southeast Brazil. *Sci. Rep.* **12**, 5836 (2022).
18. Miralles, D. G., Teuling, A. J., Van Heerwaarden, C. C. & De Arellano, J. V. G. Mega-heatwave temperatures due to combined soil desiccation and atmospheric heat accumulation. *Nat. Geosci.* **7**, 345–349 (2014).
19. Santanello, J. A. et al. Land–Atmosphere Interactions: The LoCo Perspective. *Bull. Am. Meteorol. Soc.* **99**, 1253–1272 (2018).
20. Douville, H., Ribes, A., Decharme, B., Alkama, R. & Sheffield, J. Anthropogenic influence on multidecadal changes in reconstructed global evapotranspiration. *Nat. Clim. Chang.* **3**, 59–62 (2013).
21. Libonati, R. et al. Drought–heatwave nexus in Brazil and related impacts on health and fires: A comprehensive review. *Ann. N. Y. Acad. Sci.* **n/a**.
22. IPCC: *Climate Change 2021: The Physical Science Basis. Contribution of Working Group I to the Sixth Assessment Report of the Intergovernmental Panel on Climate Change* [Masson-Delmotte, V., et al. (eds)]. Cambridge University Press, Cambridge, United Kingdom and New York, NY, USA, In press, <https://doi.org/10.1017/9781009157896>.
23. de Barros Soares, D., Lee, H., Loikith, P. C., Barkhordarian, A. & Mechoso, C. R. Can significant trends be detected in surface air temperature and precipitation over South America in recent decades? *Int. J. Climatol.* **37**, 1483–1493 (2017).
24. Regoto, P., Dereczynski, C., Chou, S. C. & Bazzanella, A. C. Observed changes in air temperature and precipitation extremes over Brazil. *Int. J. Climatol.* **41**, 5125–5142 (2021).
25. Llopert, M., Simões Reboita, M. & Porfirio da Rocha, R. Assessment of multi-model climate projections of water resources over South America CORDEX domain. *Clim. Dyn.* **54**, 99–116 (2020).
26. Reboita, M. S., Da Rocha, R. P., Dias, C. G. & Ynoue, R. Y. Climate projections for South America: RegCM3 driven by HadCM3 and ECHAM5. *Adv. Meteorol.* **2014**, (2014).
27. Chug, D., Dominguez, F. & Yang, Z. The Amazon and La Plata River Basins as Moisture Sources of South America: Climatology and Intraseasonal Variability. *J. Geophys. Res. Atmos.* **127**, 1–19 (2022).
28. Zanin, P. R. & Satyamurti, P. Hydrological processes interconnecting the two largest watersheds of South America from seasonal to intra-monthly time scales: A critical review. *Int. J. Climatol.* **40**, 3971–4005 (2020).
29. Drumond, A. et al. The role of the Amazon Basin moisture in the atmospheric branch of the hydrological cycle: a Lagrangian analysis. *Hydrol. Earth Syst. Sci.* **18**, 2577–2598 (2014).
30. Cai, W. et al. Climate impacts of the El Niño–Southern Oscillation on South America. *Nat. Rev. Earth Environ.* **1**, 215–231 (2020).
31. Taschetto, A. S. et al. ENSO Atmospheric Teleconnections. in *El Niño Southern Oscillation in a Changing Climate* 309–335 <https://doi.org/10.1002/9781119548164.ch14> (2020).
32. Grimm, A. M. Madden–Julian Oscillation impacts on South American summer monsoon season: precipitation anomalies, extreme events, teleconnections, and role in the MJO cycle. *Clim. Dyn.* **53**, 907–932 (2019).
33. Alvarez, M. S., Vera, C. S., Kiladis, G. N. & Liebmann, B. Influence of the Madden Julian Oscillation on precipitation and surface air temperature in South America. *Clim. Dyn.* **46**, 245–262 (2016).
34. Coelho, C. A. S. et al. The 2014 southeast Brazil austral summer drought: regional scale mechanisms and teleconnections. *Clim. Dyn.* **46**, 3737–3752 (2016).
35. Thielen, D. et al. The Pantanal under Siege—On the Origin, Dynamics and Forecast of the Megadrought Severely Affecting the Largest Wetland in the World. *Water* vol. 13 (2021).
36. Gomes, M. S., Cavalcanti, I. F., de, A. & Müller, G. V. 2019/2020 drought impacts on South America and atmospheric and oceanic influences. *Weather Clim. Extrem.* **34**, 100404 (2021).
37. Marengo, J. A. et al. Extreme Drought in the Brazilian Pantanal in 2019–2020: Characterization, Causes, and Impacts. *Front. Water* **3**, (2021).
38. Libonati, R. et al. Rescue Brazil's burning Pantanal wetlands. *Nature* **588**, 217–219 (2020).
39. Libonati, R. et al. Assessing the role of compound drought and heatwave events on unprecedented 2020 wildfires in the Pantanal. *Environ. Res. Lett.* <https://doi.org/10.1088/1748-9326/ac462e> (2021).
40. Qing, Y., Wang, S., Ancell, B. C. & Yang, Z.-L. Accelerating flash droughts induced by the joint influence of soil moisture depletion and atmospheric aridity. *Nat. Commun.* **13**, 1139 (2022).
41. Getirana, A., Libonati, R. & Cataldi, M. Brazil is in water crisis—it needs a drought plan. *Nature* **600**, 218–220 (2021).
42. Marengo, J. A., Douglas, M. W. & Silva Dias, P. L. The South American low-level jet east of the Andes during the 1999 LBA-TRMM and LBA-WET AMC. *campaign*. *J. Geophys. Res. Atmos.* **107**, LBA 47-1–LBA 47-11 (2002).
43. Kayano, M. T. & Andreoli, R. V. Relations of South American summer rainfall interannual variations with the Pacific Decadal Oscillation. *Int. J. Climatol.* **27**, 531–540 (2007).
44. White, R. H., Kornhuber, K., Martius, O. & Wirth, V. From Atmospheric Waves to Heatwaves: A Waveguide Perspective for Understanding and Predicting Concurrent, Persistent, and Extreme Extratropical Weather. *Bull. Am. Meteorol. Soc.* **103**, E923–E935 (2022).
45. Shimizu, M. H. & de Albuquerque Cavalcanti, I. F. Variability patterns of Rossby wave source. *Clim. Dyn.* **37**, 441–454 (2011).
46. Sousa, P. M., Blamey, R. C., Reason, C. J. C., Ramos, A. M. & Trigo, R. M. The 'Day Zero' Cape Town drought and the poleward migration of moisture corridors. *Environ. Res. Lett.* **13**, 124025 (2018).
47. NASA. La Niña times three. <https://earthobservatory.nasa.gov/images/150691/la-nina-times-three> (2022).
48. Sasaki, W., Doi, T., Richards, K. J. & Masumoto, Y. The influence of ENSO on the equatorial Atlantic precipitation through the Walker circulation in a CGCM. *Clim. Dyn.* **44**, 191–202 (2015).
49. Boers, N., Marwan, N., Barbosa, H. M. J. & Kurths, J. A deforestation-induced tipping point for the South American monsoon system. *Sci. Rep.* **7**, 41489 (2017).
50. Eiras-Barca, J. et al. Changes in South American hydroclimate under projected Amazonian deforestation. *Ann. N. Y. Acad. Sci.* **1472**, 104–122 (2020).
51. Otkin, J. A. et al. Flash Droughts: A Review and Assessment of the Challenges Imposed by Rapid-Onset Droughts in the United States. *Bull. Am. Meteorol. Soc.* **99**, 911–919 (2018).
52. Christian, J. I., Basara, J. B., Hunt, E. D., Otkin, J. A. & Xiao, X. Flash drought development and cascading impacts associated with the 2010 Russian heatwave. *Environ. Res. Lett.* **15**, 94078 (2020).
53. Montini, T. L., Jones, C. & Carvalho, L. M. V. The South American Low-Level Jet: A New Climatology, Variability, and Changes. *J. Geophys. Res. Atmos.* **124**, 1200–1218 (2019).
54. Oliveira, M. I., Nascimento, E. L. & Kannenberg, C. A New Look at the Identification of Low-Level Jets in South America. *Mon. Weather Rev.* **146**, 2315–2334 (2018).
55. Barreiro, M. & Tippmann, A. Atlantic modulation of El Niño influence on summertime rainfall over southeastern South America. *Geophys. Res. Lett.* **35**, (2008).
56. Rodrigues, R. R., Taschetto, A. S., Sen Gupta, A. & Foltz, G. R. Common cause for severe droughts in South America and marine heatwaves in the South Atlantic. *Nat. Geosci.* **12**, 620–626 (2019).
57. Gelbrecht, M., Boers, N. & Kurths, J. Phase coherence between precipitation in South America and Rossby waves. *Sci. Adv.* **4**, eaau3191 (2023).
58. Silva, G. A. M. & Ambrietti, T. Inter-El Niño variability and its impact on the South American low-level jet east of the Andes during austral summer – two case studies. *Adv. Geosci.* **6**, 283–287 (2006).
59. Wei, Y. & Ren, H.-L. Distinct MJOs Under the Two Types of La Niña. *J. Geophys. Res. Atmos.* **127**, e2022JD037646 (2022).
60. Deng, L. & Li, T. Relative roles of background moisture and vertical shear in regulating interannual variability of boreal summer intraseasonal oscillations. *J. Clim.* **29**, 7009–7025 (2016).
61. Swart, N. C., Fyfe, J. C., Gillett, N. & Marshall, G. J. Comparing trends in the southern annular mode and surface westerly jet. *J. Clim.* **28**, 8840–8859 (2015).
62. Thompson, D. W. J. et al. Signatures of the Antarctic ozone hole in Southern Hemisphere surface climate change. *Nat. Geosci.* **4**, 741–749 (2011).
63. Ruscica, R. C., Sörensson, A. A. & Menéndez, C. G. Hydrological links in Southeastern South America: soil moisture memory and coupling within a hot spot. *Int. J. Climatol.* **34**, 3641–3653 (2014).
64. Ruscica, R. C., Sörensson, A. A. & Menéndez, C. G. Pathways between soil moisture and precipitation in southeastern South America. *Atmos. Sci. Lett.* **16**, 267–272 (2015).
65. Bieri, C. A., Dominguez, F. & Lawrence, D. M. Impacts of Large-Scale Soil Moisture Anomalies on the Hydroclimate of Southeastern South America. *J. Hydrometeorol.* **22**, 657–669 (2021).
66. Ruscica, R. C., Menéndez, C. G. & Sörensson, A. A. Land surface–atmosphere interaction in future South American climate using a multi-model ensemble. *Atmos. Sci. Lett.* **17**, 141–147 (2016).
67. Olmo, M. E., Weber, T., Teichmann, C. & Bettolli, M. L. Compound Events in South America Using the CORDEX-CORE ensemble: current climate conditions and future projections in a global warming scenario. *J. Geophys. Res. Atmos.* **127**, e2022JD037708 (2022).
68. Peleg, N., Molnar, P., Burlando, P. & Fatichi, S. Exploring stochastic climate uncertainty in space and time using a gridded hourly weather generator. *J. Hydrol.* **571**, 627–641 (2019).

69. Faticchi, S. et al. Uncertainty partition challenges the predictability of vital details of climate change. *Earth's Futur.* **4**, 240–251 (2016).
70. Lee, S. et al. On the future zonal contrasts of equatorial Pacific climate: Perspectives from Observations. *Simulations, and Theories. npj Clim. Atmos. Sci.* **5**, 82 (2022).
71. Seager, R. et al. Strengthening tropical Pacific zonal sea surface temperature gradient consistent with rising greenhouse gases. *Nat. Clim. Chang.* **9**, 517–522 (2019).
72. Beck, H. E. et al. Evaluation of 18 satellite- and model-based soil moisture products using in situ measurements from 826 sensors. *Hydrol. Earth Syst. Sci.* **25**, 17–40 (2021).
73. Muñoz-Sabater, J. et al. ERA5-Land: a state-of-the-art global reanalysis dataset for land applications. *Earth Syst. Sci. Data* **13**, 4349–4383 (2021).
74. Hassler, B. & Lauer, A. Comparison of Reanalysis and Observational Precipitation Datasets Including ERA5 and WFDE5. *Atmosphere (Basel)*. **12**, (2021).
75. Coronato, T. et al. The impact of soil moisture–atmosphere coupling on daily maximum surface temperatures in Southeastern South America. *Clim. Dyn.* **55**, 2543–2556 (2020).
76. Balmaceda-Huarte, R., Olmo, M. E., Bettolli, M. L. & Poggi, M. M. Evaluation of multiple reanalyses in reproducing the spatio-temporal variability of temperature and precipitation indices over southern South America. *Int. J. Climatol.* **41**, 5572–5595 (2021).
77. Baker, J. C. A. et al. An Assessment of Land–Atmosphere Interactions over South America Using Satellites, Reanalysis, and Two Global Climate Models. *J. Hydrometeorol.* **22**, 905–922 (2021).
78. Bevacqua, E., Zappa, G., Lehner, F. & Zscheischler, J. Precipitation trends determine future occurrences of compound hot-dry events. *Nat. Clim. Chang.* **12**, 350–355 (2022).
79. Peixoto, J. P. & Oort, A. H. *American Institute of Physics. Nature* vol. 151 (1943).
80. Peixoto, J. P. Atmospheric vapor flux computations for hydrological purposes. *WMO Contrib. to Int. Hydrol. Decad.* (1973).
81. Hart, R. E. & Grumm, R. H. Using normalized climatological anomalies to rank synoptic-scale events objectively. *Mon. Weather Rev.* **129**, 2426–2442 (2001).
82. Ramos, A. M., Trigo, R. M. & Liberato, M. L. R. A ranking of high-resolution daily precipitation extreme events for the Iberian Peninsula. *Atmos. Sci. Lett.* **15**, 328–334 (2014).
83. Liberato, M. L. R. et al. Rankings of extreme and widespread dry and wet events in the Iberian Peninsula between 1901 and 2016. *Earth Syst. Dyn.* **12**, 197–210 (2021).
84. Sardeshmukh, P. D. & Hoskins, B. J. The Generation of Global Rotational Flow by Steady Idealized Tropical. *Divergence. J. Atmos. Sci.* **45**, 1228–1251 (1988).
85. Holton, J. R. & Hakim, G. J. *An introduction to dynamic meteorology: Fifth edition. An Introduction to Dynamic Meteorology: Fifth Edition* vol. 9780123848 (2012).

ACKNOWLEDGEMENTS

This work was performed under the scope of project E26/ 210.078/2023 supported by FAPERJ and under the scope of project DHEFEUS (<https://doi.org/10.54499/2022.09185.PTDC>) supported by FCT. JG and AR acknowledge FCT (Fundação para a Ciência e a Tecnologia) and I.P./MCTES for the PhD Grant 2020.05198.BD and for 2022.01167.CECCIND (Complex), respectively. RL acknowledges FAPERJ (E26/200/329/2023) and CNPq (311487/2021-1). DGM acknowledges support from the European Research Council (ERC) under grant agreement 101088405 (HEAT). AMR was

supported by the Helmholtz ‘Changing Earth’ program. LG acknowledges Xunta de Galicia, Consellería de Cultura, Educación e Universidade, under project ED431C 2021/44 ‘Programa de Consolidación e Estructuración de Unidades de Investigación Competitivas’.

AUTHOR CONTRIBUTIONS

The study was conceptualized by all authors. J.G. collected data, performed all the calculations and was responsible for the data curation and analysis. J.G. also designed all the figure and wrote the manuscript. All the authors contributed to the conception of the work, analyzed the results, wrote, reviewed and approved the final version of the manuscript.

FUNDING

Open Access was supported by national funds through FCT (PIDAAC) – UIDB/50019/2020-IDL and by <https://doi.org/10.54499/2022.09185.PTDC> (DHEFEUS).

COMPETING INTERESTS

The authors declare no competing interests.

ADDITIONAL INFORMATION

Supplementary information The online version contains supplementary material available at <https://doi.org/10.1038/s41612-023-00510-3>.

Correspondence and requests for materials should be addressed to J. L. Geirinhas.

Reprints and permission information is available at <http://www.nature.com/reprints>

Publisher's note Springer Nature remains neutral with regard to jurisdictional claims in published maps and institutional affiliations.



Open Access This article is licensed under a Creative Commons Attribution 4.0 International License, which permits use, sharing, adaptation, distribution and reproduction in any medium or format, as long as you give appropriate credit to the original author(s) and the source, provide a link to the Creative Commons license, and indicate if changes were made. The images or other third party material in this article are included in the article's Creative Commons license, unless indicated otherwise in a credit line to the material. If material is not included in the article's Creative Commons license and your intended use is not permitted by statutory regulation or exceeds the permitted use, you will need to obtain permission directly from the copyright holder. To view a copy of this license, visit <http://creativecommons.org/licenses/by/4.0/>.

© The Author(s) 2023